SARS-CoV-2 Detection Using Colorimetric Plasmonic Sensors: A Proof-of-Concept Computational Study

Somen Baidya and Ahmed M. Hassan, *Senior Member, IEEE*

***Abstract*— Traditional molecular techniques for SARS-CoV-2 viral detection are time-consuming and can exhibit a high probability of false negatives. In this work, we present a computational study of SARS-CoV-2 detection using plasmonic gold nanoparticles. The resonance wavelength of a SARS-CoV-2 virus was recently estimated to be in the near-infrared region. By engineering gold nanospheres to specifically bind with the outer surface of the SARS-CoV-2 virus, the resonance frequency can be shifted to the visible range (380 nm–700 nm). Moreover, we show that broadband absorption will emerge in the visible spectrum when the virus is partially covered with gold nanoparticles at a specific coverage percentage. This broadband absorption can be used to guide the development of an efficient and accurate colorimetric plasmon sensor for COVID-19 detection. Our observation also suggests that this technique is unaffected by the number of protein spikes present on the virus outer surface, hence can pave a potential path for a label-free COVID-19 diagnostic tool independent of the number of protein spikes.**

***Index Terms*— SARS-CoV-2, COVID-19, LSPR, plasmonic biosensor, percolation.**

I. Introduction

THE recent worldwide outbreak of novel Severe Acute Respiratory Syndrome-CoronaVirus-2 (SARS-CoV-2) has resulted in an insurmountable effect on public health and the socioeconomic aspects of modern-day life. Due to the highly contagious nature of this virus, rapid and accurate detection of SARS-CoV-2 has been the center of numerous research endeavors in the last couple of years to ensure minimal spread among the community by enforcing self-quarantine and contact tracing protocols [1]. The existing methods for SARS-CoV-2 diagnosis can be broadly categorized into following classes: (1) serological approaches, (2) molecular approaches, (3) point of care detection, (4) computerized tomography, (5) nanoscale visualization, and (6) nanophotonic biosensors [1]–[3]. Among these, reverse-transcription polymerase chain reaction (RT-PCR), a molecular technique, is considered as gold standard for SARS-CoV-2 detection from upper respiratory tract samples. Although widely adopted and authorized by US Food and Drug Administration (FDA), this technique provides some major limitations such as expensive and advanced instruments, false-positive rates, extensive and laborious sample preparation, and ssdelayed reports [2], [4], [5]. Motivated by these limitations, nanophotonic biosensor-based detections have received significant research interest due to their high sensitivity, simpler sample preparation protocols, expedited analysis time, and potential for label-free detection [4]. The majority of nanophotonic biosensors utilize the fundamental principle of the resonance oscillation of conduction electrons around nano-sized metal surfaces, known as Localized Surface Plasmons Resonance (LSPR) [1]. LSPR based biosensors exploit the enhanced near field caused by confining the electron oscillations to the nanoparticle's surface with dimensions much smaller than the incident wavelength.

Plasmonic nanoparticles have been used to accurately detect a wide range of cells and biomarkers [6]–[8]. For example, gold nanorods have been recently proposed to detect and classify macrophages, which are a kind of white cells released by the immune system [6]. Chakraborty *et al.* studied the differences in gold nanorods uptake by the M1 and M2 macrophages. They showed that the uptake of poly(allylamine hydrochloride) (PAH) coated gold nanorods by M2 macrophages was three times higher than the uptake by M1 macrophages [6]. By monitoring the scattering characteristics of the sample, this differential uptake can be used to predict the ratio of the M1 macrophages to the M2 macrophages, which can classify a wide range of infectious diseases and cancer and diagnose its current stage [6].

Gold nanoparticles have also been used to realize biological logic gates [7]. Like their electronic counterparts, biological gates are smart elements with predefined inputs and outputs [7]. The inputs can consist of an external optical or ultrasound excitation or the internal presence of a specific ion, molecule, or enzyme. The outputs can be the release/activation of an inactive drug, the release of a fluorescent signal, or the

Manuscript received 11 October 2021; revised 6 February 2022 and 21 February 2022; accepted 23 February 2022. Date of publication 2 March 2022; date of current version 30 December 2022. This work was supported in part by the University of Missouri-Kansas City. *(Corresponding author: Ahmed M. Hassan.)*

The authors are with the Department of Computer Science and Electrical Engineering, University of Missouri–Kansas City, Kansas City, MO 64110 USA (e-mail: sbg58@mail.umkc.edu; hassanam@umkc.edu).

Digital Object Identifier 10.1109/TNB.2022.3156077

aggregation/dissociation of the nanoparticles. Gold nanoparticles are particularly suited for biological gates due to their tunable optical characteristics and the capability to modify their surfaces to intelligently respond to different inputs in their environment [7].

In addition to gold nanoparticles, arrays of gold nanocavities have also been frequently used to detect biomarkers [8]. A linker is typically added to the nanocavities array to capture specific biomarkers. Arrays of nanocavities in thin gold films exhibit Surface Plasmon Resonances (SPR) which shift when the biomarker of interest is attached to the film's surface. To increase the spectral shift and increase the sensor's sensitivity, Beiderman *et al.* investigated attaching gold nanorods to the nanocavities array [8]. By adjusting the aspect ratio and the surface area of the gold nanorods, their localized surface plasmon resonance was tuned to match the resonance of the gold nanocavities, which maximized the spectral shift when they were connected. Beiderman *et al.* showed how the sensitivity of biomarker detection could be increased by combining the two plasmonic resonances modalities of cavities and nanorods [8]. Additional applications that utilize the optical properties of gold nanoparticles in biomedical application are reviewed in [9].

Since the breakout of the coronavirus pandemic in 2019, several studies have highlighted the potential of LSPR-mediated biosensor application for COVID-19 detection [1], [5], [10]–[12]. In [5], the authors were able to achieve high detection sensitivity of selected SARS-CoV-2 sequences by combining the plasmonic photothermal effect of two-dimensional gold nanoislands with LSPR sensing transduction. Djaileb *et al.* proposed a surface plasmon resonance (SPR) based sensor that can detect specific nucleocapsid antibodies present in human serum that are expressed against SAR-CoV-2 [10]. A computational model studied the detection of SARS-CoV-2 viruses augmented with gold nanorods using Surface Plasmon Polaritons (SPP) excited on a gold-coated prism [11]. In a more recent study, researchers exploited gold nanoparticle agglomeration in the presence of the target RNA sequence of SARS-CoV-2, which resulted in a 40 nm redshift in the ultraviolet-visual absorption spectrum [12]. Mahari *et al.* reported a detection scheme that employs the change in electrical conductivity of fluorine doped tin oxide electrode with gold nanoparticle due to the presence of SARS-CoV-2 antibody from spiked saliva samples [13]. Apart from these potential plasmonic applications of SARS-CoV-2 virus diagnosis, one recent study utilized the plasmonic properties of selenium nanoparticles as a labeling probe for SARS-CoV-2 antibody detection [14].

While these plasmonic biosensor studies are primarily focused on detecting specific RNA sequences of the virus or the presence of nucleocapsid antibodies due to immunogenic response of human body, the full potential of LSPR-mediated SARS-CoV-2 virus detection is still unexplored. A powerful aspect of LSPR technique is that it is highly sensitive to the assembly and morphology of the nanoparticles as well as the refractive index of the surrounding medium [15]. Consequently, inspired by the iconic solar corona-like morphology of the virus, we present a proof-of-concept computational study on the colorimetric detection of SARS-CoV-2 virus without additional steps of sample preparation like most of the previously mentioned diagnostic approaches. A theoretical study recently reported that a SARS-CoV-2 virus demonstrates strong resonance characteristics at specific mid-infrared wavelengths independent of the background host [16]. Utilizing LSPR fundamentals, we demonstrate that these resonance characteristics could be shifted to the visible range for potential colorimetric detection of SARS-CoV-2 viruses in a liquid. In this work, colorimetry indicates that the sensing modality studied has the potential to generate clear color changes that can be detected by the naked eye when the SARS-CoV-2 virus is present.

This paper is arranged as follows. Section II discusses the proposed sensing modality and the computational techniques employed. Section III presents the computational results and Section IV summarizes the Conclusions and Future Work.

II. Methodology

A. Localized Surface Plasmon Resonance

Nanoparticles composed of noble metal, such as gold and silver, experience Localized Surface Plasmon Resonances (LSPR) with significant amplification of the fields in the vicinity of the nanoparticle [11], [17]. In the far field, the LSPR are reflected as resonances in the absorption cross-section of the nanoparticles. These resonances are highly sensitive to the environment of the nanoparticle and has been proposed as a sensing modality for a wide range of applications including the detections of single cells and various other biomarkers [17], [18].

If multiple nanoparticles are fabricated, the LSPR frequency is highly dependent on the shape, size, the distribution of the nanoparticles as well as their environment [8]. Due to the recent advances in fabrication technology of noble metal nanostructures, nanoparticles with precise shapes, sizes, and distributions have been fabricated for use as biosensors in multiple applications [19]–[25].

B. Computational Model Development

1) Effective Medium Properties: A simplified two-dimensional structural view of a SARS-CoV-2 virus is shown in Fig. 1 [3]. Overall, the virus has the typical coronavirus features with four types of proteins, namely, nucleocapsid (N), membrane (M) protein, envelop (E) protein and spike protein (S) [26]. The most popular entry mechanism of SARS-CoV-2 virus in humans is through the attachment of the spike protein onto the angiotensin-converting enzyme 2 (ACE2) receptor on the surface of host cells. Our hypothesis is based on the existence of appropriate antisense oligonucleotides (ASOs) specific for S-protein, so that the AuNPs can attach to the receptors when capped with these suitable ASOs (shown in Fig. 1) [12]. A detailed description of the virus preparation and funtionalizing the gold nanoparticle agglomerate for SARS-CoV-2 specific N-gene sequence with selected ASOs, can be found elsewhere [12]. However, due to the unexplored nature of the virus genome, there is a gap in existing literature regarding to the appropriate choice of ASO or virus-binding

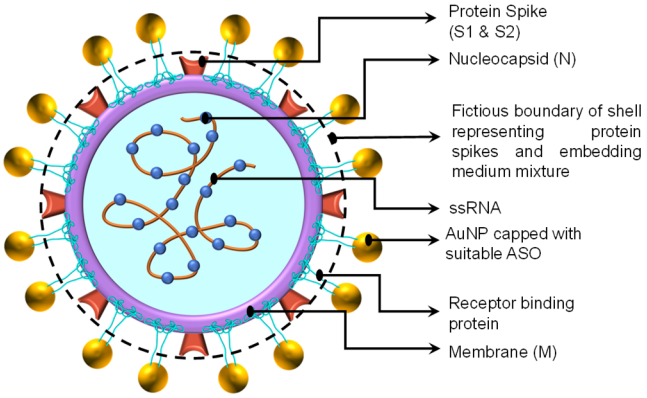

Fig. 1. A simplified structure of the SARS-CoV-2 virus coated with AuNPs based on our hypothetical sensing modality.

antibodies specific to SARS-CoV-2 virus. Also, this specific direction is out of the reach of our study. Interested readers are referred to the review of [4], where the author has presented an excellent overview of existing literatures on nanomaterials-based detection format (namely immobilization strategy or biological receptor) for different target viruses.

On average, the diameter of a SARS-CoV-2 is 100-125 nm with ∼100 spikes, 9 nm to 12 nm length [3], [27]. Since our main interest in in the visible range (∼380 nm – 700 nm), the protein spikes will be significantly smaller than the incident wavelength [16]. The protein spikes do not fully cover the virus and some of the embedding medium, assumed to be water in this work, will exist between the spikes. Due to their small sizes relative to the incident wavelengths, the protein spikes and the embedding medium can be modeled as a homogenous shell [16].The shell will be treated as a composite with an effective permittivity (ϵ_s) that can be calculated as follows (1) [16]:

$$\epsilon_s = (1-p)\,\epsilon_b + p\epsilon_c \tag{1}$$

where ϵ_c and ϵ_b are the dielectric constants of the protein spikes and background medium, respectively, and p is the percentage of the shell volume occupied by the spikes [16]. In this work, both the protein spikes and the virus's core are assigned the same dielectric properties following [16]. Besides, in all of the following results, the embedding medium is assumed to be water and, therefore, ϵ_b, is assigned the dielectric properties of water. Assuming, the overall geometry has 120 nm diameter including the protein spike length (∼10 nm), the volume of the shell that includes the spikes would be $\frac{4}{3}\pi(60^3 - 50^3)$ nm^3 and the corresponding volume for each spike is $\frac{1}{3}\pi\left(5^2\right)10$ nm^3 (assuming that each spike have a conical shape with 10 nm height and 5 nm radius). Since there are 100 spike per virus on average, the approximate filling factor of the protein spike in the shell that cover the SARS-CoV-2 virus would be $p \approx \frac{100\times(\frac{1}{3}\pi(5^2)10)}{\frac{4}{3}\pi(60^3-50^3)} \approx 0.0687$. This volume fraction is lower than the 0.5 value reported in the seminal work in [16]. However, it is based on recent SARS-CoV-2 characterization measurements which indicate a much fewer number of protein spikes than previously expected [27]. In this work we investigate both protein spikes volume fraction of $p \approx 0.0687$ and $p \approx 0.5$ to investigate the effect of different number of protein spikes per virus. Fig. 2 shows a comparison of the relative dielectric permittivity of the SARS-CoV-2 core and the relative dielectric permittivity of the shell that is composed of a mixture of protein spikes and water. For the dielectric properties of the shell, different p values, are presented in Fig. 2.

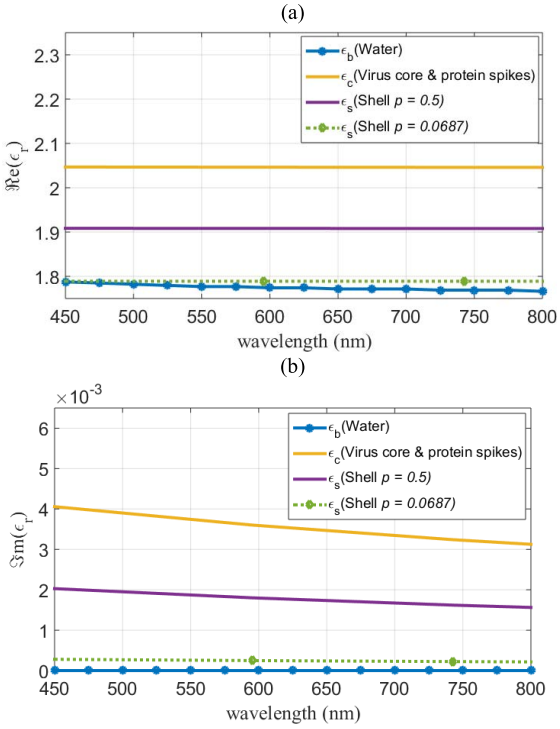

Fig. 2. Comparison of the (a) real, (b) imaginary part of the relative permittivity of core and shell model of SARS-CoV-2 with two specific filling factors of $p = 0.5$ and $p = 0.0687$ with respect to the dielectric properties of AuNP.

2) 3D Finite Element Model: The sensing mechanism reported in this work is based on the selective attachment of a particular number of spherical AuNP to the SARS-CoV-2. This is feasible due to recent fabrication and functionalization techniques (see for example [12]. We considered spherical AuNPs with 10 nm radius similar to the structures available in [28]. Unless specified otherwise, we will use $p = 0.5$. We investigated the effect of different numbers of AuNPs attached to each virus on the optical scattering characteristics. For meshing and computational issues, the AuNP spheres are set not to overlap and a negligible 0.5 nm separation between each AuNP and the virus shell are inserted (Fig. 3). We primarily studied the absorption cross-section (ACS) ans scattering cross-section (SCS) of the overall assembly of the virus covered by the AuNPs. ACS is a quantitative measure of the resistive losses of an irradiated nanostructure and SCS is the is a quantity proportional to the rate at which a particular radiation–target interaction occurs, both can be evaluated from (2) and (3) [29], [30]:

$$C_{ACS} = \frac{1}{2S_0}\iiint Re\left(\boldsymbol{J}.\boldsymbol{E}^*\right)dV \tag{2}$$

$$C_{SCS} = -\frac{\omega}{2S_0}\iiint Im\left(\Delta\epsilon\left(\boldsymbol{E}_b+\boldsymbol{E}_s\right).\boldsymbol{E}_{\boldsymbol{b}}^*\right)dV - C_{ACS} \tag{3}$$

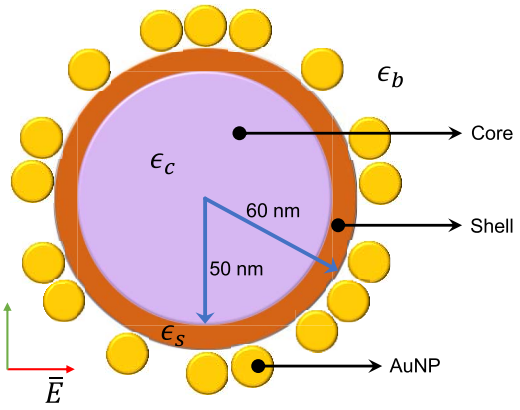

Fig. 3. A sketch of the LSPR sensing mechanimsm implemented for the detection of the SARS-CoV-2 virus with core radius 50 nm and shell radius 60 nm. The shell represents a mixture of the virus's protein spikes and the embedding medium set to water in this work following [16].

where $\boldsymbol{E}$ is the total electrical field that can be calculated as the summation of the incident/background $\boldsymbol{E}_b$ of angular frequency ω and scattered $\boldsymbol{E}_s$ fields, $\boldsymbol{J}$ is the current density, S_0 is the time-averaged Poynting vector of the incident plane-wave and V is the volume of the overall virus-AuNPs assembly.

The computational modeling of this assembly was performed using the frequency-domain electromagnetics wave (*emw*) module of the finite-element-based COMSOL Multiphysics solver [31]. The dimensions of the shell considered for our computational study can accommodate a maximum 152 AuNPs of 10 nm radius on the surface of the virus. We analyzed the ACS of the overall structure for four AuNP percentage surface coverages (10%, 25%, 60%, and 100%) under plane-wave excitation. The percentage corresponds to the number of NPs attached. That is 10%, 25%, 60%, and 100% percentage coverage correspond to 15, 38, 91, and 152 AuNPs, respectively, attached to the virus's surface. To incorporate the randomness in AuNP distribution on the virus shell, we used 5 different AuNP configurations for each percentage surface coverage where the number of AuNps were kept constant, but their locations on the surface of the virus were varied. The average ACS of these ten configurations was calculated for each coverage percentage in the visible range, between free-space wavelengths of 450 nm – 800 nm.

III. Result and Discussion

We present the optical ACS area of our model for 10%, 25%, and 60% AuNP coverage in Fig. 4(a), Fig. 4(b), & Fig. 4(c) respectively. The legends (v1-v5) and ($v1_{pp}$-$v5_{pp}$) correspond to the five random combinations of AuNP when the incident electric field is y-polarized and z-polarized, respectively. In all cases, the propagation direction of the incident plane wave is along the x-axis. All simulations were performed on a Dual Intel Xeon Processor E5-2698 64-core processor with 2.30 GHz processor base frequency. The average computational time for the simulation of each configuration ranged from 15 hours to 98 hours based on the number of AuNPs.

The average ACS for the 10% and 25% AuNP coverage exhibits a resonance wavelength at 525 nm with a narrow bandwidth. This is similar to the resonance frequency response of a single AuNP in water as reported in [29]. When the surface coverage of the virus is 10%, the distance between the AuNPs is relatively large, and therefore, we should only exhibit the AuNP resonance of the dilute limit where the interactions between the AuNPs are negligible.

As we increase the percentage surface coverage, the interaction between the AuNPs are no longer negligible and this is demonstrated in the increase in the BW of the ACS. In the in case of 25% AuNP coverage (Fig. 4(b)), the ACS shows a wider bandwidth than the 10% case. The average ACS for the 60% AuNP coverage shows the maximum bandwidth that spans the wavelengths of ∼450 nm to 725 nm. For the 60% surface coverage, the AuNPs are forced into close proximity as they are attached to the small surface of the virus. Therefore, the AuNPs start exhibiting strong electromagnetic interactions. When the surface coverage of the AuNPs is close to the percolation threshold, a broadband response is exhibited similar to what was found in planar heterogeneous gold distributions [32]. Fig. 5 summarizes the results in Fig. 4 by showing the average ACS for the 10%, 25%, and 60% coverage cases. To put the results in Fig. 5 into context, consider the case where a certain liquid needs to be tested for the presence or absence of the SARS-CoV-2 viruses. A moderate concentration of spherical AuNPs, chemically modified to target the virus's antigens, can be added to the liquid and the color of the liquid monitored. If there are no viruses in the liquid, the AuNP will remain widely separated, causing only an ACS absorption near 525 nm, the color of green-blue, and therefore, the liquid will appear red in color. If there are SARS-CoV-2 in the liquid, a broadband absorption in the visible spectrum will occur, giving the liquid a dark blackish color as shown in the 60% ACS in Fig. 5. Therefore, our computational experiments predict that the virus can be rapidly detected by inspecting the liquid's color after adding the AuNps and without the use of additional equipment. A similar phenomenon was experimentally observed in detecting exosomes, which are biological vesicles similar in size to viruses [34]. Our study provides a computational explanation of the broadband ACS phenomenon exhibited in exosomes and it shows that it can also be extended to the SARS-CoV-2 virus.

Fig. 5 also shows the normalized ACS for the 100% coverage case where the surface of the virus is completely covered by AuNPs. However, for the 100% coverage, the normalized ACS does not show the same broadband behavior of the 60%. This can be explained by the plasmon resonance hybridization discussed in detail in [33]. Briefly, for gold shells surrounding a dielectric core, phase retardation effects can cause the distribution of charge on the inner and outer layer of the gold shell to hybridize, leading to two resonances [33]. The difference in the charge distribution between the two resonances causes the ACS to be maximum at one resonance and the Scattering Cross Section (SCS) to be maximum at the second resonance.

To show that a similar phenomenon occurs in a SARS-CoV-2 virus covered with AuNps. Fig. 6 shows the

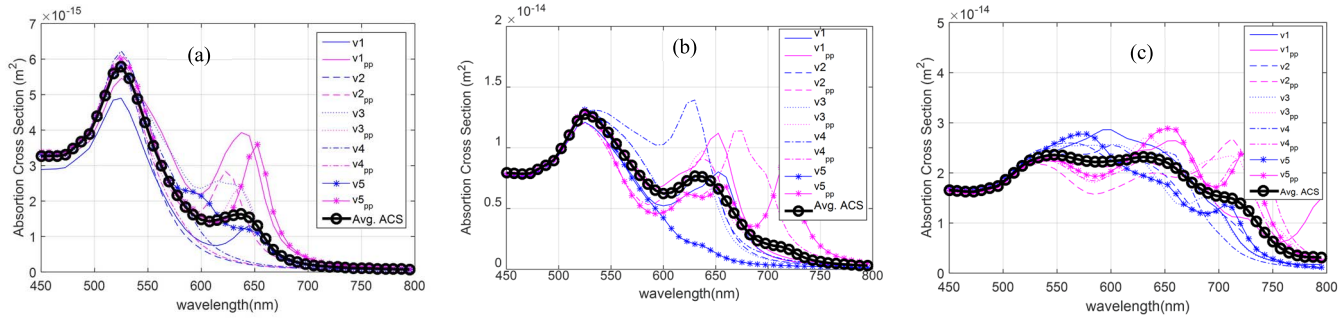

Fig. 4. Absorption cross-sectional area (ACS) for three cases of AuNP coverage (a) 10% surface coverage, (b) 25% surface coverage, and (c) 60% surface coverage.

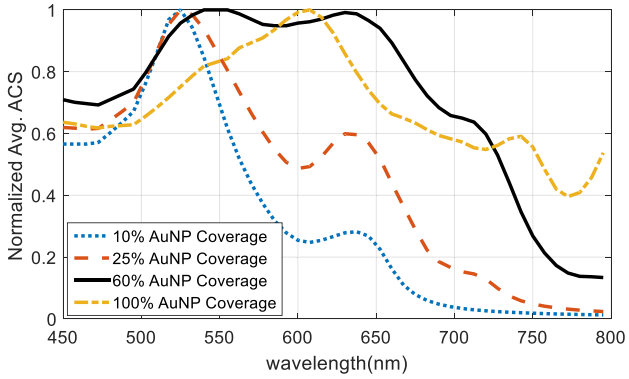

Fig. 5. A comparison of the absorption characteristics when the virus surface is covered 10%, 25%, 60% and 100% by AuNPs. Normalized ACS for all 4 cases demonstrates a broadband response when60% of the surface of the virus is covered with AuNPs.

average ACS and SCS for 3 different percentage surface coverage: 10%, 60%, and 100%. Fig. 6(a) shows that for the 10% case, the number of AuNPs is small, causing a small interaction between the virus-AuNP agglomerate and the incident wave. For the 60% case, many AuNPs are attached to the virus's surface, but there are still gaps between the different AuNPs. These gaps are of different size and they allow incident wave of a wide range of wavelengths to penetrate the virus-AuNPs agglomerate. The penetrating waves will then experience multiple reflections confining the energy in the virus-AuNp agglomerate leading to the broadband ACS shown in the inset of Fig. 6(b). When the AuNPs fully cover the virus, as shown in Fig. 6(c), wavelengths larger than 630 nm cannot penetrate the virus-AuNp aggolemerate and are simply reflected by the AuNPs that now now form a tight layer around the virus. Beyond 630 nm, Fig. 6(c) shows that the ACS decreases and the SCS increases as the incident radiation fails to penetrate the virus-AuNPs agglomerate and is simply reflected from the outer surface. Therefore, an important recommendation from this computational feasibility study is to design the AuNPs to bind with an antigen of the SARS-CoV-2 that allows for partial coverage, ideally 60% coverage, of the virus to achieve an ACS with the widest bandwidth.

Further, we investigated the effect of change in protein spike filling factor on the ACS spectrum for the same configuration of SARS-CoV-2 by incorporating a realistic filling factor of $p = 0.0687$ in stead of $p = 0.5$ used in all previous results. Varying p, will change ϵ_s, according to (1), which represents the dielectric properties of the shell that represents the mixture of the protein spikes and the embedding medium, water in this case. In Fig. 7, we demonstrate the comparison between two ACS spectra for a specific configuration of 60% AuNP coverage. From Fig. 2(a), we can highlight the changes of SARS-CoV-2 shell dielectric properties as the real part of the relative permittivity value drops from 1.9 to ∼1.8 (5% reduction). However, the relative permittivity of the AuNPs is much higher than the dielectric properties of the shell. Consequently, the ACS spectrum is dominated by the AuNP configurations only and we do not observe any significant change in the absorbance as we change the number of protein spikes per SARS-CoV-2 virus. Based on this observation, we can hypothesize that any variation in the number of spike proteins or the dielectric properties of the core of the virus will not affect the performance of our proposed LSPR-mediated colorimetric sensing technique.

Future work will involve studying how the structure of the AuNP affects the broadband absorption when the virus is partially covered. Spherical AuNPs are symmetric, and therefore we only need to study variations in their locations on the surface of the virus and the overall coverage percentage. Any other shape will require studying the variations in the orientation of the AuNPs in addition to their location and the percentage coverage of the virus' surface. For example, gold nanorods are asymmetric which causes them to exhibit both longitudinal and/or transverse resonances based on their orientation [6], [8]. Therefore, the orientation of each gold nanorod on the surface of the virus needs to be varied to follow what happens in experiments. This randomness in orientation might enhance the bandwidth of the broadband absorption similar to what was reported in other kinds of nanostructures [35], [36]. Finally, for gold nanorods, the surface area and the aspect ratio play a significant role in their optical characteristics [6], [8]. These two parameters will also be tuned to maximize the broadband absorption when the virus is partially covered. Another important class of nanoparticles is the superballs, which have a normalized equation similar to that of a sphere but with a variable exponent, m such that $|x|^m + |y|^m + |z|^m = 1$ [37]. For a sphere, $m = 2$, but a wide range of shapes can be achieved from the same equation by assigning different real values to m. These superball shapes range from octahedral structures when $m \leq 1$ all the way

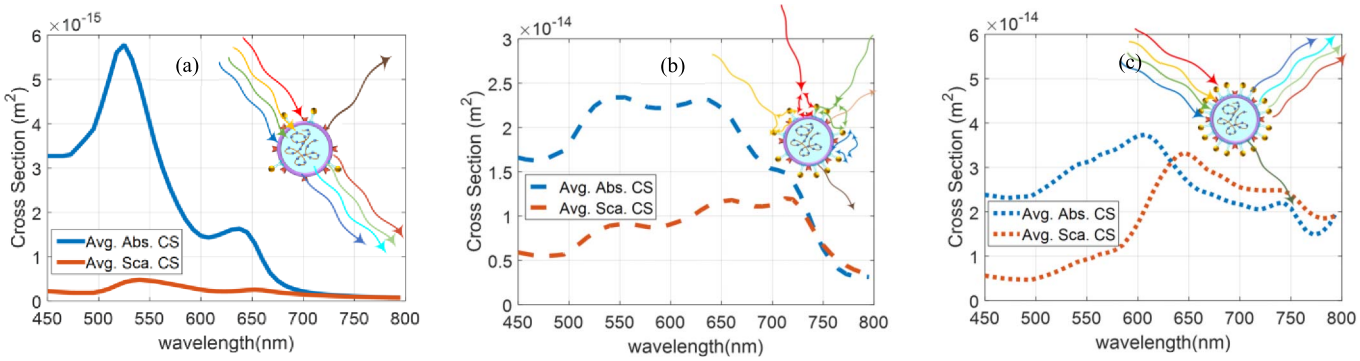

Fig. 6. Comparison of average absorption cross-section (ACS) and scattering cross-sectional (SCS) area for (a) 10%, (b) 60%, and (c) 100% surface coverage along with the prominent scattering phenomena depicted inset for each individual case (a) transmission, (b) absorption, and (c) reflection.

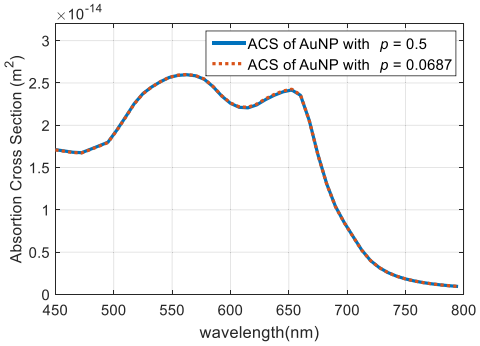

Fig. 7. Comparison of the absorption characteristics when the protein spike filling factor is changed from 0.5 to 0.0687. Only one configuration of 60% AuNP coverage is depicted here for two separate filling factors.

to cubes when $m = \infty$. The exponent m can be used as a continuous shape parameter to generate trends that clarify how the broadband absorption varies with shape. Moreover, the packing of superballs has been recently a topic of extensive studies [38]. We can also perform similar packing studies of superball nanostructures around the virus and show how this packing will affect the broadband response. Investigating all of the previous studies will require numerous lengthy computational simulations. But optimizing these parameters will enhance the broadband absorption, which will further increase the sensitivity of the proposed sensing modality and facilitate its adoption.

IV. Conclusion

In this work, we used computational simulations to prove that plasmonic resonances can be utilized to detect the SARS-CoV-2 virus. The detection mechanism is based on the emergence of a broadband absorption in the visible spectrum when gold nanoparticles are designed to partially cover the virus. The detection technique described in this work can be used independently or hybridized with traditional detection techniques to improve their accuracy. In the future, we want to carry out more AuNP coverage percentages to help design a precise and optimized platform that can elicit expected broadband response. Moreover, varying the shape and size of the AuNPs will be investigated to further optimizate the accuracy of the proposed technique.

References

[1] M. Soler, M. C. Estevez, M. Cardenosa-Rubio, A. Astua, and L. M. Lechuga, "How nanophotonic label-free biosensors can contribute to rapid and massive diagnostics of respiratory virus infections: COVID-19 case," *ACS Sensors*, vol. 5, no. 9, pp. 2663–2678, Sep. 2020, doi: 10.1021/acssensors.0c01180.

[2] A. Eftekhari *et al.*, "A comprehensive review of detection methods for SARS-CoV-2," *Microorganisms*, vol. 9, no. 2, p. 232, Jan. 2021, doi: 10.3390/microorganisms9020232.

[3] N. Bhalla, Y. Pan, Z. Yang, and A. F. Payam, "Opportunities and challenges for biosensors and nanoscale analytical tools for pandemics: COVID-19," *ACS Nano*, vol. 14, no. 7, pp. 7783–7807, Jul. 2020, doi: 10.1021/acsnano.0c04421.

[4] E. Mauriz, "Recent progress in plasmonic biosensing schemes for virus detection," *Sensors*, vol. 20, no. 17, p. 4745, Aug. 2020, doi: 10.3390/s20174745.

[5] G. Qiu, Z. Gai, Y. Tao, J. Schmitt, G. A. Kullak-Ublick, and J. Wang, "Dual-functional plasmonic photothermal biosensors for highly accurate severe acute respiratory syndrome coronavirus 2 detection," *ACS Nano*, vol. 14, no. 5, pp. 5268–5277, May 2020, doi: 10.1021/acsnano.0c02439.

[6] R. Chakraborty, D. Leshem-Lev, R. Kornowski, and D. Fixler, "The scattering of gold nanorods combined with differential uptake, paving a new detection method for macrophage subtypes using flow cytometery," *Nano Lett.*, vol. 20, no. 11, pp. 8360–8368, Nov. 2020, doi: 10.1021/acs.nanolett.0c03525.

[7] E. A. Barnoy, R. Popovtzer, and D. Fixler, "Fluorescence for biological logic gates," *J. Biophoton.*, vol. 13, no. 9, Sep. 2020, Art. no. e202000158, doi: 10.1002/jbio.202000158.

[8] M. Beiderman *et al.*, "Optimization of gold nanorod features for the enhanced performance of plasmonic nanocavity arrays," *ACS Omega*, vol. 6, no. 43, pp. 29071–29077, Nov. 2021, doi: 10.1021/acsomega.1c04301.

[9] L. Wang, M. H. Kafshgari, and M. Meunier, "Optical properties and applications of plasmonic-metal nanoparticles," *Adv. Funct. Mater.*, vol. 30, no. 51, Dec. 2020, Art. no. 2005400, doi: 10.1002/adfm.202005400.

[10] A. Djaileb *et al.*, "A rapid and quantitative serum test for SARS-CoV-2 antibodies with portable surface plasmon resonance sensing," ChemRxiv, Cambridge Open Engage, Cambridge, U.K., Apr. 2020, doi: 10.26434/chemrxiv.12118914.v1.

[11] C. M. Das *et al.*, "Gold nanorod assisted enhanced plasmonic detection scheme of COVID-19 SARS-CoV-2 spike protein," *Adv. Theory Simul.*, vol. 3, no. 11, Nov. 2020, Art. no. 2000185, doi: 10.1002/adts.202000185.

[12] P. Moitra, M. Alafeef, K. Dighe, M. B. Frieman, and D. Pan, "Selective naked-eye detection of SARS-CoV-2 mediated by N gene targeted antisense oligonucleotide capped plasmonic nanoparticles," *ACS Nano*, vol. 14, no. 6, pp. 7617–7627, Jun. 2020, doi: 10.1021/acsnano.0c03822.

[13] S. Mahari, A. Roberts, D. Shahdeo, and S. Gandhi, "eCovSens-ultrasensitive novel in-house built printed circuit board based electrochemical device for rapid detection of nCovid-19 antigen, a spike protein domain 1 of SARS-CoV-2," BioRxiv, Cold Spring Harbor Lab., New York, NY, USA, Tech. Rep. 2020.04.24.059204, 2020, doi: 10.1101/2020.04.24.059204.

[14] C. Chen *et al.*, "Rapid detection of anti-SARS-CoV-2 antibody using a selenium nanoparticle-based lateral flow immunoassay," *IEEE Trans. Nanobiosci.*, vol. 21, no. 1, pp. 37–43, Jan. 2022, doi: 10.1109/TNB.2021.3105662.

[15] L. M. Liz-Marzán, "Tailoring surface plasmons through the morphology and assembly of metal nanoparticles," *Langmuir*, vol. 22, no. 1, pp. 32–41, Jan. 2006, doi: 10.1021/la0513353.

[16] C. Valagiannopoulos and A. Sihvola, "Maximal interaction of electromagnetic radiation with corona virions," *Phys. Rev. B, Condens. Matter*, vol. 103, no. 1, Jan. 2021, Art. no. 014114, doi: 10.1103/PhysRevB.103.014114.

[17] V. Amendola, R. Pilot, M. Frasconi, O. M. Maragò, and M. A. Iatì, "Surface plasmon resonance in gold nanoparticles: A review," *J. Phys., Condens. Matter*, vol. 29, no. 20, Apr. 2017, Art. no. 203002, doi: 10.1088/1361-648X/aa60f3.

[18] C. L. Wong and M. Olivo, "Surface plasmon resonance imaging sensors: A review," *Plasmonics*, vol. 9, no. 4, pp. 809–824, Aug. 2014, doi: 10.1007/s11468-013-9662-3.

[19] E. Hutter and J. H. Fendler, "Exploitation of localized surface plasmon resonance," *Adv. Mater.*, vol. 16, no. 19, pp. 1685–1706, Oct. 2004, doi: 10.1002/adma.200400271.

[20] K. M. Mayer and J. H. Hafner, "Localized surface plasmon resonance sensors," *Chem. Rev.*, vol. 111, no. 6, pp. 3828–3857, Jun. 2011, doi: 10.1021/cr100313v.

[21] M.-Q. He, Y.-L. Yu, and J.-H. Wang, "Biomolecule-tailored assembly and morphology of gold nanoparticles for LSPR applications," *Nano Today*, vol. 35, Dec. 2020, Art. no. 101005, doi: 10.1016/j.nantod.2020.101005.

[22] B. Sepúlveda, P. C. Angelomé, L. M. Lechuga, and L. M. Liz-Marzán, "LSPR-based nanobiosensors," *Nano Today*, vol. 4, no. 3, pp. 244–251, Jun. 2009, doi: 10.1016/j.nantod.2009.04.001.

[23] C. Liu, C. C. Mi, and B. Q. Li, "Energy absorption of gold nanoshells in hyperthermia therapy," *IEEE Trans. Nanobiosci.*, vol. 7, no. 3, pp. 206–214, Sep. 2008, doi: 10.1109/TNB.2008.2002284.

[24] M. S. Khan, G. Varshney, and P. Giri, "Altering the multimodal resonance in ultrathin silicon ring for tunable THz biosensing," *IEEE Trans. Nanobiosci.*, vol. 20, no. 4, pp. 488–496, Oct. 2021, doi: 10.1109/TNB.2021.3105561.

[25] D. Vijayalakshmi, C. T. Manimegalai, N. Ayyanar, D. Vigneswaran, and K. Kalimuthu, "Detection of blood glucose with hemoglobin content using compact photonic crystal fiber," *IEEE Trans. Nanobiosci.*, vol. 20, no. 4, pp. 436–443, Oct. 2021, doi: 10.1109/TNB.2021.3097343.

[26] M. A. Shereen, S. Khan, A. Kazmi, N. Bashir, and R. Siddique, "COVID-19 infection: Emergence, transmission, and characteristics of human coronaviruses," *J. Adv. Res.*, vol. 24, pp. 91–98, Jul. 2020, doi: 10.1016/j.jare.2020.03.005.

[27] Y. M. Bar-On, A. Flamholz, R. Phillips, and R. Milo, "SARS-CoV-2 (COVID-19) by the numbers," *eLife*, vol. 9, p. e57309, Mar. 2020, doi: 10.7554/eLife.57309.

[28] *NIST—SRM Order Request System RM 8012—Gold Nanoparticles, Nominal 30 nm Diameter*. Accessed: Jul. 19, 2021. [Online]. Available: https://www-s.nist.gov/srmors/view_detail.cfm?srm=8012

[29] L. Jauffred, A. Samadi, H. Klingberg, P. M. Bendix, and L. B. Oddershede, "Plasmonic heating of nanostructures," *Chem. Rev.*, vol. 119, no. 13, pp. 8087–8130, Jul. 2019, doi: 10.1021/acs.chemrev.8b00738.

[30] Q. Bai, M. Perrin, C. Sauvan, J.-P. Hugonin, and P. Lalanne, "Efficient and intuitive method for the analysis of light scattering by a resonant nanostructure," *Opt. Exp.*, vol. 21, no. 22, pp. 27371–27382, Nov. 2013, doi: 10.1364/OE.21.027371.

[31] *COMSOL Multiphysics*, COMSOL AB, Stockholm, Sweden. Accessed: Dec. 2020. [Online]. Available: https://www.comsol.com

[32] J. Obrzut, J. F. Douglas, O. Kirillov, F. Sharifi, and J. A. Liddle, "Resonant microwave absorption in thermally deposited Au nanoparticle films near percolation coverage," *Langmuir*, vol. 29, no. 28, pp. 9010–9015, Jul. 2013, doi: 10.1021/la401753y.

[33] C. Ayala-Orozco *et al.*, "Au nanomatryoshkas as efficient near-infrared photothermal transducers for cancer treatment: Benchmarking against nanoshells," *ACS Nano*, vol. 8, no. 6, pp. 6372–6381, Jun. 2014, doi: 10.1021/nn501871d.

[34] D. Maiolo *et al.*, "Colorimetric nanoplasmonic assay to determine purity and titrate extracellular vesicles," *Anal. Chem.*, vol. 87, no. 8, pp. 4168–4176, Apr. 2015, doi: 10.1021/ac504861d.

[35] S. Dey, E. J. Garboczi, and A. M. Hassan, "Electromagnetic resonance analysis of asymmetric carbon nanotube dimers for sensing applications," *Nanotechnology*, vol. 31, no. 42, Aug. 2020, Art. no. 425501, doi: 10.1088/1361-6528/aba058.

[36] A. M. Hassan, F. Vargas-Lara, J. F. Douglas, and E. J. Garboczi, "Electromagnetic scattering from multiple single-walled carbon nanotubes having tumbleweed configurations," *IEEE Trans. Antennas Propag.*, vol. 65, no. 6, pp. 3192–3202, Jun. 2017, doi: 10.1109/TAP.2017.2691475.

[37] D. J. Audus, A. M. Hassan, E. J. Garboczi, and J. F. Douglas, "Interplay of particle shape and suspension properties: A study of cube-like particles," *Soft Matter*, vol. 11, pp. 3360–3366, Apr. 2015, doi: 10.1039/C4SM02869D.

[38] Y. Jiao, F. H. Stillinger, and S. Torquato, "Optimal packings of superballs," *Phys. Rev. E, Stat. Phys. Plasmas Fluids Relat. Interdiscip. Top.*, vol. 79, no. 4, Apr. 2009, Art. no. 041309, doi: 10.1103/PhysRevE.79.041309.